AGU PUBLICATIONS

Geochemistry, Geophysics, Geosystems

RESEARCH ARTICLE
10.1002/2016GC006514

Tectonic structure of the Mid-Atlantic Ridge near 16°30′N

Ross Parnell-Turner[1], Hans Schouten[1], and Deborah K. Smith[1]

[1]Department of Geology and Geophysics, Woods Hole Oceanographic Institution, Woods Hole, Massachusetts, USA

Key Points:
- Multibeam bathymetry, gravity and magnetic data acquired at 16°30′N, Mid-Atlantic Ridge
- Misalignment between axis and magnetic anomalies shows reorganization since 780 ka
- Structural variability indicates changes in spreading style over short, 1–2 Ma timescales

Correspondence to:
R. Parnell-Turner,
rparnellturner@whoi.edu

Citation:
Parnell-Turner, R., H. Schouten, and D. K. Smith (2016), Tectonic structure of the Mid-Atlantic Ridge near 16°30′N, *Geochem. Geophys. Geosyst.*, *17*, 3993–4010, doi:10.1002/2016GC006514.

Received 13 JUL 2016
Accepted 27 SEP 2016
Accepted article online 4 OCT 2016
Published online 22 OCT 2016

Abstract The 16°30′N area of the Mid-Atlantic Ridge represents an area of present-day detachment faulting. Here we present shipboard bathymetric, magnetic and gravity data acquired up to 65 km from the ridge axis that reveal a varied tectonic history of this region. Magnetic data are used to calculate spreading rates and examine spreading rate variability along and across the axis. Bathymetric and gravity data are used to infer the crustal structure. A central magnetic anomaly 40% narrower than expected is observed along much of the study area. Misalignment between modern-day spreading center and magnetic anomalies indicates tectonic reorganization of the axis within the past 780 ka. Observed magnetic anomalies show a pattern of anomalous skewness consistent with rotation of magnetic vectors probably associated with detachment faulting. Relatively thin crust north of a small (~7 km) nontransform offset coincides with a weakly magmatic spreading axis. In contrast, to the south a robust axial volcanic ridge is underlain by thicker crust. Variations in crustal structure perpendicular to the axis occur over tens of kilometers, indicating processes which occur over timescales of 1–2 Ma.

1. Introduction

At slow-spreading mid-ocean ridges, slip on low-angle faults, known as detachments, can accommodate a significant portion of relative plate motion [e.g., *Cannat et al*., 1995; *Cann et al*., 1997; *Tucholke et al*., 1998; *Smith et al*., 2008]. Where these faults continue to slip for long time periods, lower crustal and mantle rocks are exhumed to form oceanic core complexes [*Tucholke and Lin*, 1994; *Cannat et al*., 2006; *Baines et al*., 2008]. Detachment faulting is also associated with uneven, irregular seafloor terrain and asymmetric plate accretion, thought to be explained by limited magmatism [*Lagabrielle et al*., 1998; *Searle et al*., 2003; *Okino et al*., 2004; *Buck et al*., 2005; *Tucholke et al*., 2008; *Mallows and Searle*, 2012]. Plate spreading accommodated by detachments may occur over millions of years, leading to broad expanses of oceanic crust being formed this way [*Karson*, 1999; *Schroeder and Cheadle*, 2007; *Escartin et al*., 2008]. For example, up to half of the length of the Mid-Atlantic Ridge (MAR) between 12°30′N and 35°N is thought to exhibit detachment-mode spreading on at least one side of the axis [*Escartin et al*., 2008].

Here we present a detailed study of the crustal structure of a segment of the slow-spreading MAR near 16°30′N (Figure 1). The MAR between 12°N and 17°N is thought to be spreading at a full rate of 25 km Ma^{-1} [*DeMets et al*., 2010], and is flanked by broad areas of blocky seafloor terrain, typical of detachment fault activity [*Macleod et al*., 2002; *Fujiwara et al*., 2003; *Smith et al*., 2006, 2008, 2014]. We use bathymetric, magnetic and gravity data to establish the history of plate spreading in this region under the influence of detachment faulting. Our observations constrain the spatial and temporal variations in tectonic style and provide an insight into the relationships between spreading style and crustal accretion. Near the spreading axis we investigate the character of the central magnetic anomaly, which shows considerable cross-axis asymmetry. Away from the spreading axis, we find variations in relative crustal thickness both parallel and perpendicular to the ridge axis.

2. Tectonic Setting and Geologic Features

Smith et al. [2014] provided a detailed description of the bathymetric and tectonic character of the 16°30′N region. The study area consists of two spreading segments, separated by a ~7 km nontransform offset (NTO) near 16°42′N (Figure 1), which is not associated with a recognizable off-axis trace in the bathymetry or the magnetic anomalies discussed later.

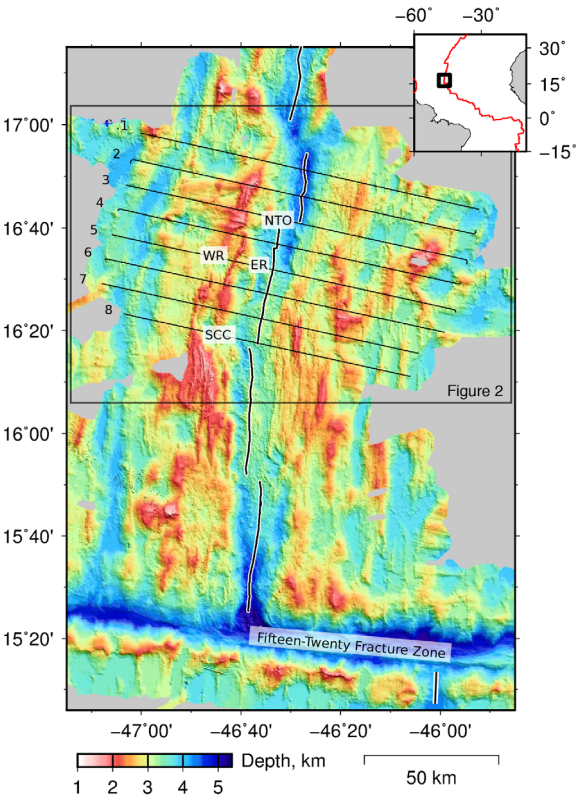

Figure 1. Location map (inset) and compilation of multibeam bathymetric data from study area (Cruises KN182-03 [*Smith et al.*, 2006], YK98-05 [*Fujiwara et al.*, 2003], and KN210-05 [*Smith et al.* 2014]). Numbered black lines are geophysical data acquisition track lines, KN210-05; black/white line marks ridge axis; SCC is South Core Complex; WR is West Ridge; ER is East Ridge; NTO marks nontransform offset, box shows location of Figure 2.

In the southern part of the study area, bathymetric data reveal a classic domed, corrugated detachment fault called South Core Complex (SCC; Figure 1). The termination of this fault is located ~6.5 km west of the volcanic spreading axis and its footwall scarp is characterized by corrugations 400–1600 m in wavelength [*Smith et al.*, 2014]. The top of a 9 km-long normal fault scarp, called East Ridge, is located about 6 km west of the volcanic axis to the northeast of SCC. Another fault scarp, called West Ridge, is located ~15 km west of the volcanic axis, and consists of a ~21 km-long, ~1 km-wide bathymetric high bounded on the east by normal faulting dipping toward the axis (Figure 1) [*Smith et al.*, 2014]. West Ridge has been interpreted as the breakaway of an outwardly rotated long-lived detachment fault [*Smith et al.*, 2008]. Seafloor to the north and west of West Ridge is uneven and occasionally corrugated, suggesting it was also generated during detachment faulting. Similar corrugations, elongated parallel to the spreading direction, can also be identified to the east of the spreading axis. Rock samples dredged up to 20 km west of the ridge axis reveal abundant gabbro and peridotite lithologies [*Smith et al.*, 2014]. These observations, in addition to bathymetric mapping, provided additional constraints to show that large portions of the seafloor have been formed by slip along detachment faults.

Earthquake seismicity is common in the 16°30′N area, demonstrated by a two-year deployment of an autonomous hydrophone array which detected ~500 earthquakes (M_w 2–3) between 16°N and 17°N [*Smith et al.*, 2003]. This high rate of seismicity is indicative of present-day slip on numerous detachment faults [*Escartin et al.*, 2008]. Further evidence for active detachment faults today is provided by the progressive thinning of sediments toward the termination of an exposed detachment fault footwall at 16°35′N, 46°35′W observed on subbottom profiles acquired using AUV *Sentry* [*Parnell-Turner et al.*, 2014].

3. Data Acquisition and Processing

Bathymetric, magnetic and gravity data were acquired simultaneously in May 2013 during R/V *Knorr* Cruise KN210-05. Ship track lines were oriented parallel to the plate spreading flowlines (~105°) [*DeMets et al.*, 1990] and spaced roughly 10 km apart (Figure 1). Track lines extend ~65 km either side of the spreading axis and assuming an average total spreading rate of ~25 km Ma^{-1}, the survey covers crust up to ~5 Ma in age [*DeMets et al.*, 1990].

3.1. Bathymetric Data

Multibeam bathymetric data were acquired using the hull-mounted SeaBeam 3012-P1 system, which has 121 beams operating at 12 kHz and a swath width of up to 120°. Spatial resolution is typically 100–150 m depending on water depth, and sound velocity calibration was achieved using an expendable bathythermograph (XBT) deployed at 16° 55.9′N 47° 8.9′W. Multibeam data were processed using MB-System software [*Caress and Chayes*, 1996]. The data have minimal spurious returns and artifacts, most of which were removed using automated algorithms. Bathymetric data from KN210-05 were merged with data from

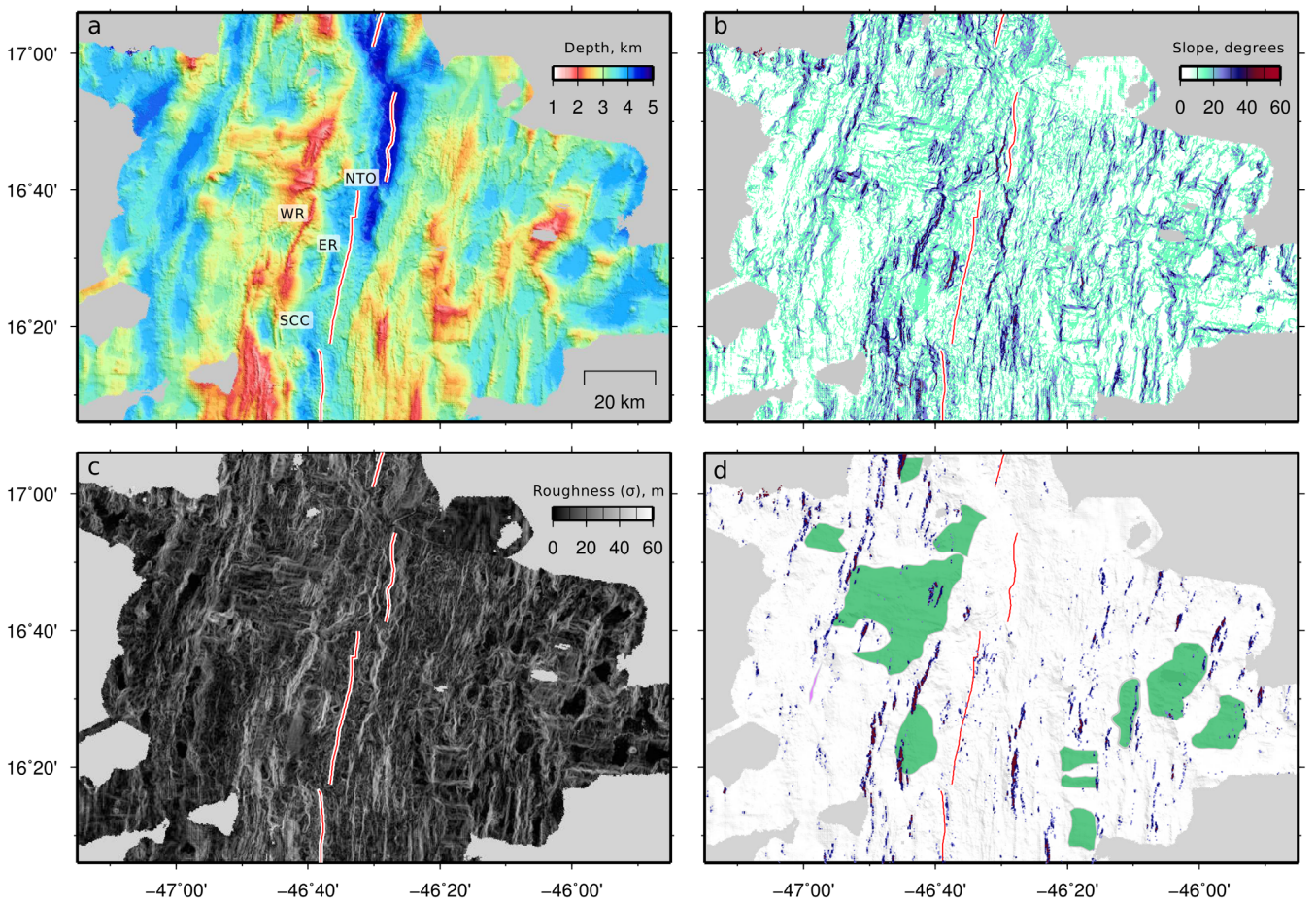

Figure 2. Bathymetric terrain analysis and interpretation. (a) Multibeam bathymetry. Red/white line marks ridge axis; SCC is South Core Complex; WR is West Ridge; ER is East Ridge; NTO marks nontransform offset. (b) Slope gradient. (c) Seafloor roughness, defined as standard deviation of slope gradient. (d) Geologic interpretation draped over bathymetry. Green polygons are corrugated seafloor (following *Smith et al.* [2014]); colored dots mark outward-facing slopes with angle >20°.

previous surveys (Cruises KN182-03 [*Smith et al.*, 2006] and YK98-05 [*Fujiwara et al.*, 2003]) to yield continuous coverage from the Fifteen Twenty Fracture Zone to ~17°N (Figure 1).

Slope gradient and seafloor roughness grids were obtained from the final bathymetric data set in order to interpret the gross tectonic features (Figure 2). Seafloor roughness was estimated using the standard deviation of the slope gradient calculated within a 200 m window [*Micallef et al.*, 2007]. Slope gradient is a useful aid in identification of outward-facing slopes (i.e., slopes dipping away from the spreading axis), which are typically associated with detachment faults. Pillow lavas with equant geometry have been identified on the 20° outward-facing slope of East Ridge using towed camera images [*Smith et al.*, 2008]. This observation led *Smith et al.* [2008] to conclude that these outward facing slopes are back-tilted sections of originally subhorizontal axial valley floor. After fault initiation, slip continues and the valley floor material, forming a breakaway, is flexurally rotated away from the axis, eventually becoming a steep outward-facing slope [e.g., *Buck*, 1988]. Seafloor roughness (Figure 2c), combined with the illuminated bathymetric grid, is used to identify corrugations oriented parallel to the spreading direction, typical of detachment faulted terrain (Figure 2d).

3.2. Magnetic Anomaly Data

Sea surface magnetic data were acquired using a Marine Magnetics SeaSPY Overhauser total field magnetometer. This sensor was towed 300 m behind the stern of the vessel at a speed of ~10 kts (~5 m s^{-1}) and data were recorded at a sampling interval of 1 s. The magnetic anomaly was calculated by subtracting the International Geomagnetic Reference Field (IGRF) model from the measured field [*Finlay et al.*, 2010] and the effects of diurnal variation were removed using a straight-line de-trending algorithm.

3.3. Gravity Data

Gravity data were acquired using a Bell BGM-3 gravimeter at a sampling interval of 1 s. Base station absolute gravity ties were made at stations in Bridgetown, Barbados and Woods Hole, MA, USA. After applying a 360 s Gaussian filter and Eötvös correction, the free-air anomaly (FAA) was calculated by subtracting observed values from the International Gravity Formula 1980.

4. Magnetic Anomalies and Crustal Magnetization

Near-axis magnetic anomaly identification in this region is challenging due to sparse data coverage, slow spreading rates, low latitude and complex interaction between magmatic and tectonic plate spreading styles. Magnetic anomalies older than polarity chron C2 times (>1.3 Ma) are more symmetric and provide a useful starting point for our analysis [*Fujiwara et al*., 2003]. Regional magnetic anomaly profiles that intersect track lines from KN210-05 were acquired as part of the Caribbean-Atlantic Geotraverse Project (CAG71) on board National Oceanographic and Atmospheric Administration Ship (NOAAS) *Researcher* in September-November 1971 (National Geophysical Data Center) [*Peter et al*., 1973]. These data provide useful context for data collected during KN210-05 (Figure 3a). During CAG71, ship position was fixed at 2 h intervals using a Doppler satellite system and magnetic data were recorded every 60s using an instrument towed 215 m behind the ship. These acquisition parameters are likely to have caused some artifacts in the data. Nonetheless, these additional data allow tentative identification of magnetic anomalies up to polarity chron 6A times (∼20.5 Ma). Polarity chrons were identified along two of these regional lines (CAG71-1 and -2, Figures 3b and 3c) using the geomagnetic reversal timescale of *Cande and Kent* [1995]. Chron picks from CAG71

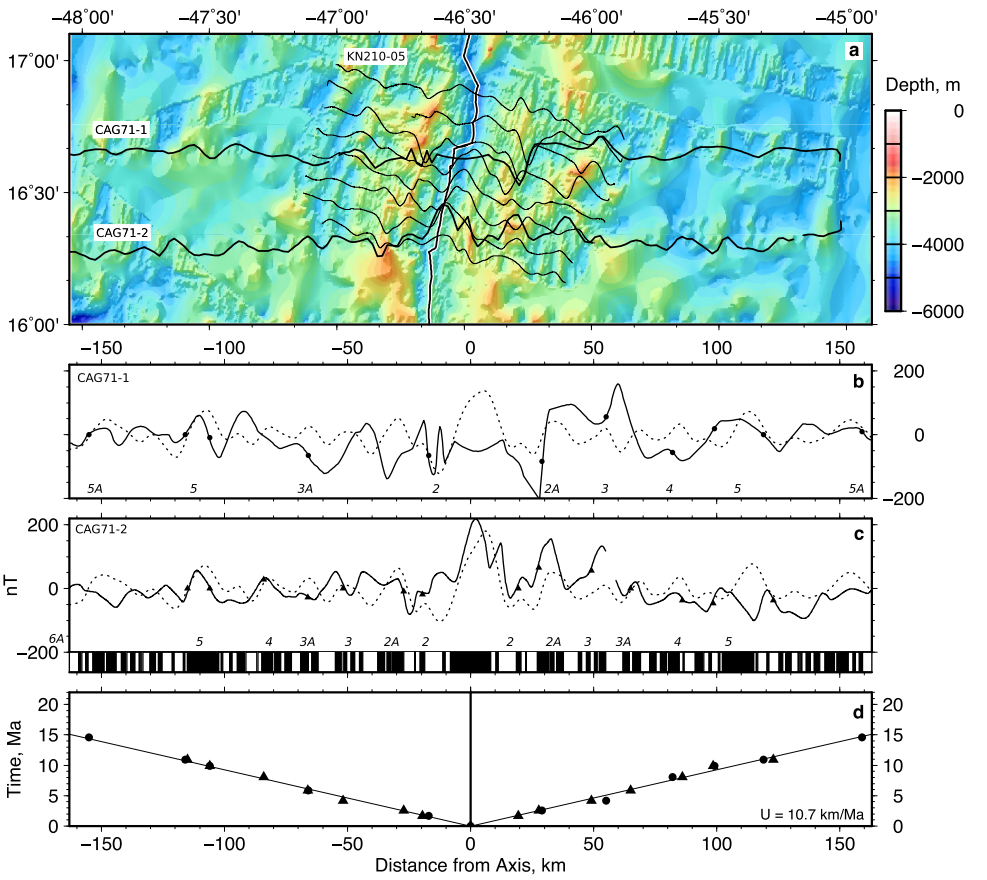

Figure 3. Regional bathymetric map with magnetic anomaly profiles. (a) Thick black lines are magnetic profiles from NOAAS *Researcher* Cruise CAG71; thin black lines are magnetic profiles from KN210-05; black/white line is ridge axis. (b and c) Solid black lines are magnetic anomaly profiles CAG71-1 and CAG71-2; dashed line is modeled magnetic anomaly. Magnetic polarity blocks plotted beneath assuming full spreading rate of 22.4 mm/yr. Labeled circles/triangles are picked chrons. (d) Spreading rate history from CAG71 data. Circles/triangles are picks from CAG71-1 and −2, respectively, solid line is best-fitting least-squares regression. Half spreading rate, *U*, noted.

profiles were fitted to a straight line using ordinary least-squares regression, to yield an apparent total spreading rate of 21.4 km Ma^{-1} (Figure 3d). This rate is slower the 25 km Ma^{-1} rate predicted by global plate motion models (MORVEL) [*DeMets et al*., 2010]. In order to verify this discrepancy, we calculated synthetic magnetic anomalies using the program MODMAG [*Mendel et al*., 2005]. We assume a magnetized layer of thickness 1.0 km and model the transition zone between adjacent inversely magnetized blocks using a contamination coefficient of 0.8 [*Tisseau and Patriat*, 1981; *Mendel et al*., 2005]. Blocks in the model are assumed to have acquired magnetization at a latitude of 16°30′N and at have an orientation of 010°. There is a fair match between the observed and predicted anomalies (Figure 3b): chrons 5 and 6 show good agreement on the western side of both lines, while there is a good match for anomaly 2A on either side of the axis for both lines. Although the fits to other chrons are more variable in quality, the data from CAG71 support our initial interpretation and reflect a full spreading rate of 21.4 km Ma^{-1}. Hence these regional data provide additional constraints on identification of younger chrons (e.g., 2A and 3) along KN210-05 profiles.

Magnetic anomaly profiles from KN210-05 are shown in Figures 4a and 5. Individual magnetic polarity chrons are difficult to identify, so we began with comparison to the CAG71 profiles. Our method for magnetic chron identification was also informed by patterns in crustal magnetization, similar to the approach used by *Fujiwara et al*. [2003]. We also tested the use of the analytic function to aid in identification of magnetized block edges [*Nabighian*, 1972]. This method did not improve our ability to identify polarity chrons, possibly due to the complex geometry and rotation of magnetized bodies in the area.

4.1. Crustal Magnetization

Crustal magnetization was calculated to correct for the effects of bathymetry and remove skewness due to the low magnetic latitude of our study area, using a Fourier inversion method [*Parker and Huestis*, 1974]. The inversion procedure was performed using the gridded magnetic anomaly data assuming a uniform, 1 km thick magnetic source layer beneath the seafloor. Within the source layer, direction of magnetization was taken to be parallel to a geocentric dipole field and a tapered cosine bandpass filter was used to remove wavelengths less than 7 km and greater than 50 km. No annihilator was added to the data during the inversion, the resulting magnetization grid is shown in Figure 4b. We identified the volcanic axis based on bathymetric character, often marked by an axial volcanic ridge (AVR), which we take to represent the locus of most recent spreading. Preliminary chron boundary locations were identified based upon zero-crossings in the magnetization grid (Figure 4b).

4.2. Central Magnetic Anomaly

The central, Bruhnes, anomaly has a median width of 10.0 km and shows considerable variation in amplitude and character between profiles. This width is little more than half of that typically expected at a spreading rate of 21.4 km Ma^{-1}. North of the NTO at 16°42′N, the Bruhnes anomaly is low in amplitude ($<$ 200 nT) with minima near the axis (lines 1, 2 and 3, Figure 4a). Magnetization of the central anomaly along profiles 1 and 2 is relatively low, with values of $\sim$2 A/m (Figure 4b). The central magnetization high on these two profiles is located 2–4 km to the east of the volcanically defined spreading axis. Immediately north of the NTO, the central magnetization high on line 3 is centered on the spreading axis but is likely contaminated by the NTO. The NTO has an offset of $\sim$7 km, which is not reflected in the C1n.o and older chrons in Figure 4b. This observation suggests a recent reorganization of the axis that occurred sometime after 0.78 Ma. In the southern area (lines 4 to 8), the central magnetization high shows consistent cross-axis asymmetry, with the maximum amplitude located 2–4 km east of the volcanic spreading axis, similar to that seen on lines 1 and 2. The Bruhnes anomaly on lines 3, 4 and 5 has the strongest positive magnetization intensity with amplitudes of 3–4 A/m.

4.3. Chron Identification and Spreading Rate Analysis

Refined magnetic chron boundaries were picked based upon the character of anomalies shown in Figure 5. Pick identification was guided by initial identifications from the magnetization inversion (Figure 4b) and intersections with CAG71 profiles (Figure 3). In order to verify and refine our picks, we used MODMAG to calculate synthetic magnetic anomaly profiles [*Mendel et al*., 2005]. Chron picks are plotted as a function of time versus distance from axis in Figure 6, and listed in Table 1. Half-spreading rates were obtained by fitting a regression model by method of ordinary least-squares to the C1n.o and older picks on the eastern side of the axis. Anomalies on the eastern flank are clearer than those on the western flank and allow a

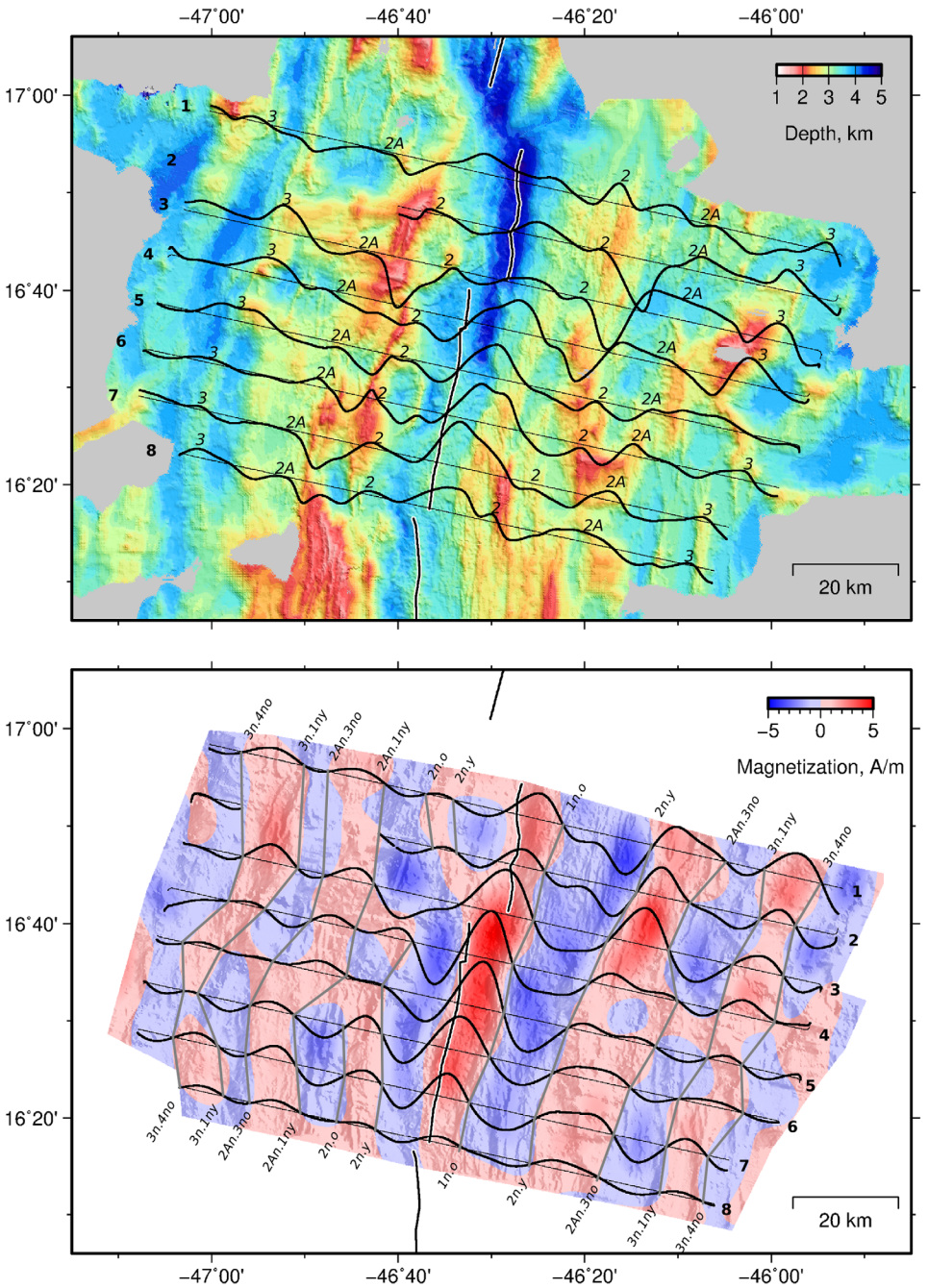

Figure 4. Magnetic anomalies, bathymetry and crustal magnetization. (a) Bathymetric map with magnetic anomaly profiles. Numbered thin black lines show ship track lines; thick black lines are magnetic anomaly profiles with selected magnetic chron labels (italicized); black/white lines mark ridge axis. (b) Crustal magnetization illuminated with bathymetric slope. Bold black lines are magnetization profiles; labeled gray lines show chron boundaries identified by magnetization zero-crossings.

definition of the expected location of crust of zero age (i.e., x axis intercept). This intercept represents the location of zero-age if no recent reorganization of the axis had taken place. Picks west of the axis were then fitted with the additional constraint of the intercept calculated from the eastern side. The common intercept produces a model of constant total spreading until the present. Our fitting procedure reveals a pattern of slightly asymmetric spreading up to Bruhnes-Matuayma times (C1n.o; 780 ka) and considerable and variable asymmetric spreading after Brunhes-Matuyama due to the recent reorganization of the spreading axis. This asymmetry is manifest by the expected zero-age intercept to be offset from the modern-day volcanic

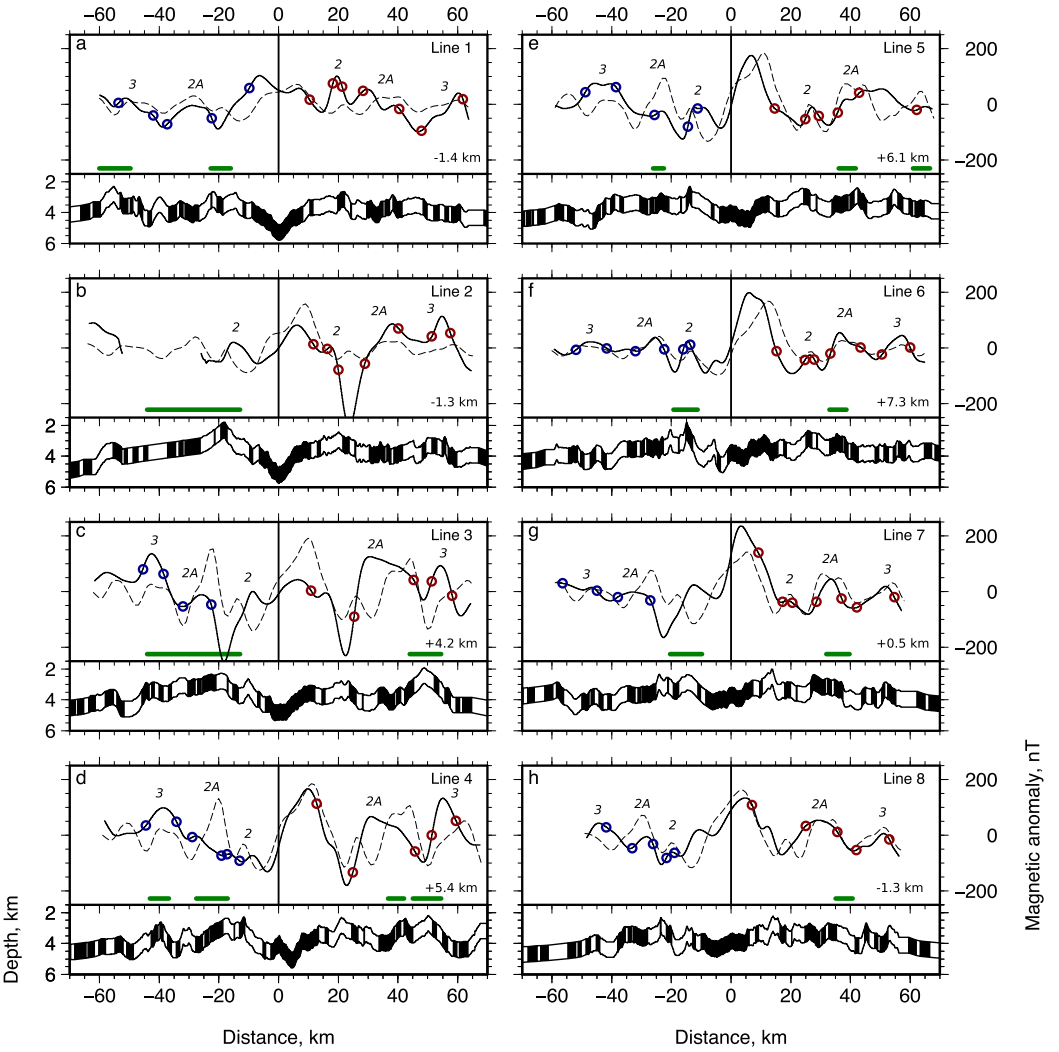

Figure 5. (a–h) Magnetic anomaly data and models for lines 1–8, respectively. Solid black lines are observed magnetic anomaly, dashed lines are modeled magnetic anomaly. Italicized labels indicate selected magnetic chrons. Models calculated using spreading rates obtained in Figure 6 and variable offsets between central anomaly, offset distances noted in km (positive indicates eastward shift). Horizontal green lines show extent of corrugated seafloor from Figure 2d. Black/white polygons show seafloor bathymetric profile and magnetized blocks used in model.

spreading center, by distances up to 7.3 km (line 6). We include these offsets in our synthetic anomaly models, but not the recent severe and asymmetric spreading, because the whole reorganization took place within the Brunhes normal period and does not affect the placement of the B/M boundaries in the models. We assume a magnetized layer of thickness 1.0 km and use the geomagnetic polarity timescale of *Cande and Kent* [1995]. We model the transition zone between adjacent inversely magnetized blocks using a contamination coefficient of 0.8 [*Tisseau and Patriat*, 1981; *Mendel et al.*, 2005]. Blocks in the model are assumed to have acquired magnetization at a latitude of 16°30′N and have an orientation of 010°. Model blocks and resulting calculated magnetic profiles are shown in Figure 5.

The positions of old/young boundaries in the models agree well with those observed, in particular for areas in which corrugated seafloor is not seen (e.g., eastern side of lines 5–8; Figure 5). Areas where corrugations are present show less satisfactory agreement between model and data (e.g., western side of lines 3 and 4). Anomalies on the eastern side of the axis match the model fairly well even in the presence of (presumably extinct) detachment faults. On the western side, where detachment faulting activity may be younger and still active, the agreement between model and data is less good. Phases of the observed anomalies for chrons 2A and 3 do not closely match those predicted by the model in a number of places. On the eastern

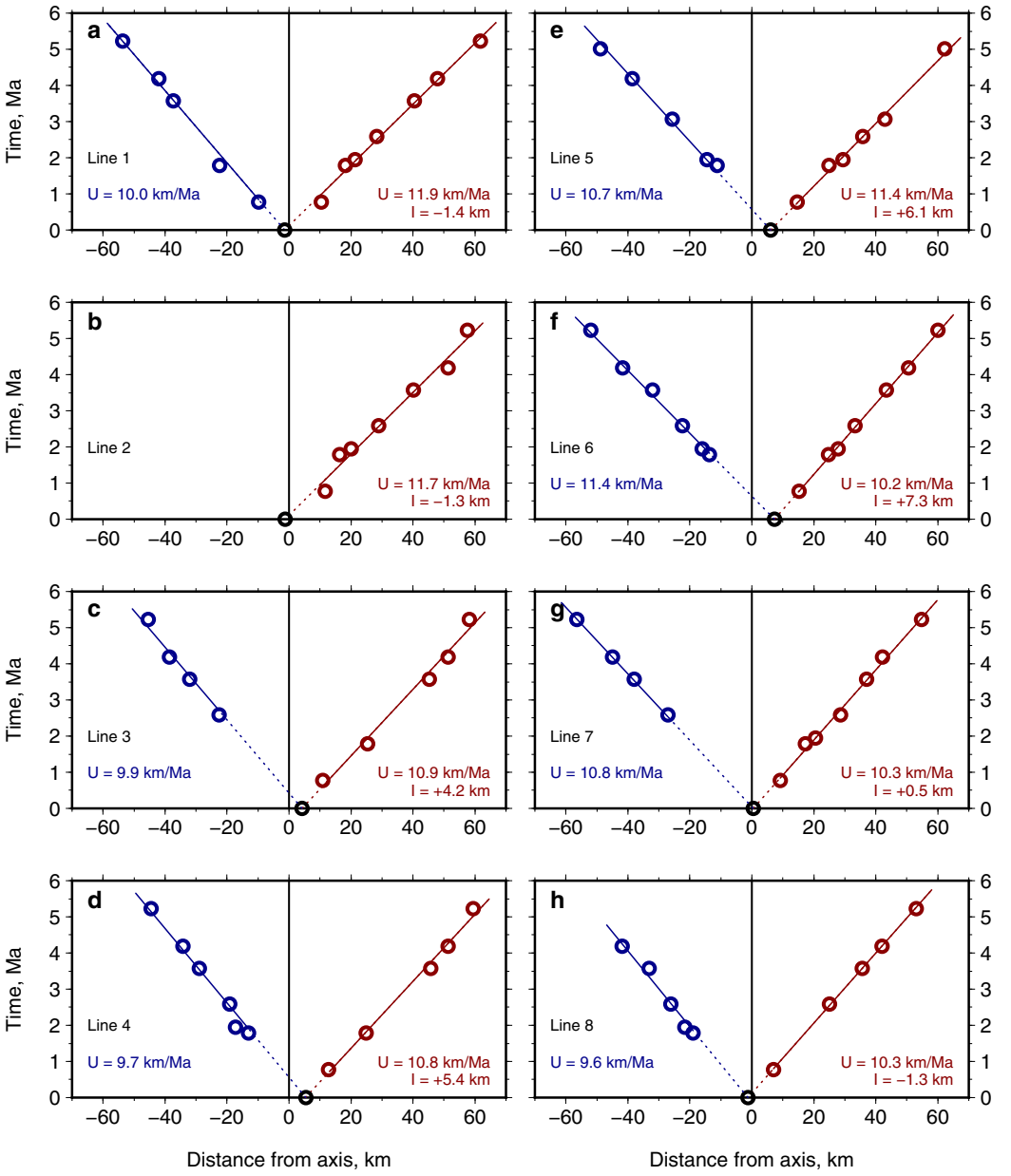

Figure 6. Spreading rate analysis for lines 1–8. (a–h) Red/blue circles are magnetic anomaly picks east/west of axis, respectively; black circles are zero-age intercept; solid lines show best-fitting least-squares regression, dotted lines show fit extrapolated to zero-age intercept obtained from eastern picks. Half spreading rates, *U*, obtained from regression east and west of axis, and distance axis intercepts, *I*, noted.

side of line 6, for example, chron 2A is predicted to be symmetrical in shape, whereas the observed anomaly for chron 2A is asymmetric in shape (Figure 5f). This difference is consistent with a clockwise rotation about a horizontal axis parallel to the rift valley walls of the remnant magnetization vector. On the western side of line 6, the phase shift between observed and calculated anomalies for chron 2A implies counterclockwise rotation. Similar sense of phase shift can be seen for chron 3, with the magnetic anomaly sources to the east apparently rotated clockwise, and those to the west rotated counterclockwise. Similarly, on the eastern side of lines 5 and 7, a comparison between modeled and observed individual positive anomalies appears to reveal a clockwise phase shift for chrons 2A and 3.

The mean half spreading rate to the east of the axis is 10.9 ± 0.7 km Ma^{-1} (where error is 1 σ). West of the axis, spreading rates are slightly lower, with a mean of 10.3 ± 0.7 km Ma^{-1}. Mean total spreading rate for all lines is 21.2 ± 0.6 km Ma^{-1}. This rate is in good agreement with that obtained from the regional CAG71

Table 1. Magnetic Anomaly Picks[a]

	Chron	1n.o	2n.y	2n.o	2An.1ny	2An.3no	3n.1ny	3n.4no
	Age, Ma	0.78	1.77	1.95	2.58	3.58	4.18	5.23
Line 1	east	10.4	18.2	21.3	28.4	40.5	47.9	61.8
	west	9.8	22.4	–	–	37.4	42.0	53.6
Line 2	east	11.7	16.4	20.0	28.9	40.2	51.4	57.6
	west							
Line 3	east	10.9	25.3			45.3	51.8	58.2
	west				22.6	32.1	38.5	45.5
Line 4	east	12.8	24.9			45.7	51.4	59.5
	west		13.1	17.3	19.1	28.9	34.2	44.5
Line 5	east	14.6	24.9	29.4	35.7	46.0	–	62.3
	west		11.2	14.5		25.6	38.5	48.9
Line 6	east	15.2	24.8	27.9	33.3	43.4	50.6	60.0
	west		13.7	16.0	22.5	32.0	41.7	51.9
Line 7	east	9.1	17.3	20.6	28.6	37.1	42.2	54.7
	west				27.0	38.0	45.0	56.4
Line 8	east	71			25.1	35.6	42.0	53.0
	west		19.0	21.7	26.2	33.2	41.8	–

[a]Distances given in km east/west from ridge axis, chron ages from [*Cande and Kent*, 1995].

data set, and is also lower than that predicted by global plate motion models (MORVEL) [*DeMets et al*., 2010]. In the area immediately to the north of Fifteen-Twenty Fracture Zone at 15°30′N, *Fujiwara et al*. [2003] report a total spreading rate of 25.1 ± 0.7 km Ma^{-1}. Higher rates of up to 26.0 ± 0.9 km Ma^{-1} are reported by *Fujiwara et al*. [2003] in their S1 segment just south of the Fifteen-Twenty Fracture Zone, centered at 14°45′N. Observed magnetic anomalies in this study region cannot be explained by the faster spreading rates of 25 km Ma^{-1} suggested by *Fujiwara et al*. [2003] north of the Fifteen-Twenty Fracture Zone. Magnetic anomalies north of the Fifteen-Twenty Fracture Zone are atypical in character and difficult to interpret. Despite the detailed data acquisition and analysis by *Fujiwara et al*. [2003], this ambiguous magnetic anomaly character may have led to increased uncertainty in their spreading rate estimates, perhaps explaining the discrepancy. Alternatively, the North American-South American plate boundary may be located between the Fifteen-Twenty Fracture Zone and 16°N, allowing the possibility of different spreading rates north and south of the fracture zone [*Roest and Collette*, 1986].

5. Gravity Anomalies and Crustal Structure

5.1. Gravity Anomaly Analysis

Free-air gravity anomaly observations primarily reflect variations in seafloor topography (Figure 7a). In order to account for subsurface density variations, we calculated mantle Bouguer and residual mantle Bouguer anomalies (MBA and RMBA, respectively) using the approach of *Kuo and Forsyth* [1988] and *Prince and Forsyth* [1988]. The MBA was calculated by removing the gravitational effects of the water-crust and crust-mantle interfaces using an upward-continuation method assuming a crustal thickness of 5 km [*Parker*, 1973]. The resulting MBA map (Figure 7b) primarily reflects variations in mantle thermal structure and variations in the thickness and/or density of the crust [*Kuo and Forsyth*, 1988; *Lin et al*., 1990]. The RMBA was obtained by applying a thermal correction to the MBA in order to account for the gravitational effects of upwelling and cooling of mantle material at the mid-oceanic ridge and associated transform faults. This thermal correction was calculated using the three-dimensional passive upwelling approach of *Phipps Morgan and Forsyth* [1988] which takes into account the effects of the Fifteen-Twenty Fracture Zone to the south, results plotted in Figure 7c. The resulting RMBA map is shown in Figure 7d, which represents crustal density anomalies and deviations from the assumed crustal thickness of 5 km.

Regional variations in crustal thickness can be inferred by assuming that the RMBA is solely produced by spatial variation in crustal thickness. We define crustal material as having a uniform density of 2700 kg m^{-3}, which may include serpentinized peridotite, basalt and gabbro. Hence this method yields an upper bound of magmatic crustal thickness. Relative crustal thickness, tc_r, was calculated by downward continuation of the RMBA, assuming a reference crustal thickness, tc_{ref}, of 5 km [*Parker and Huestis*, 1974; *Kuo and Forsyth*, 1988]. During the inversion, wavelengths $>$ 35 km were removed with a low-pass filter and cosine taper

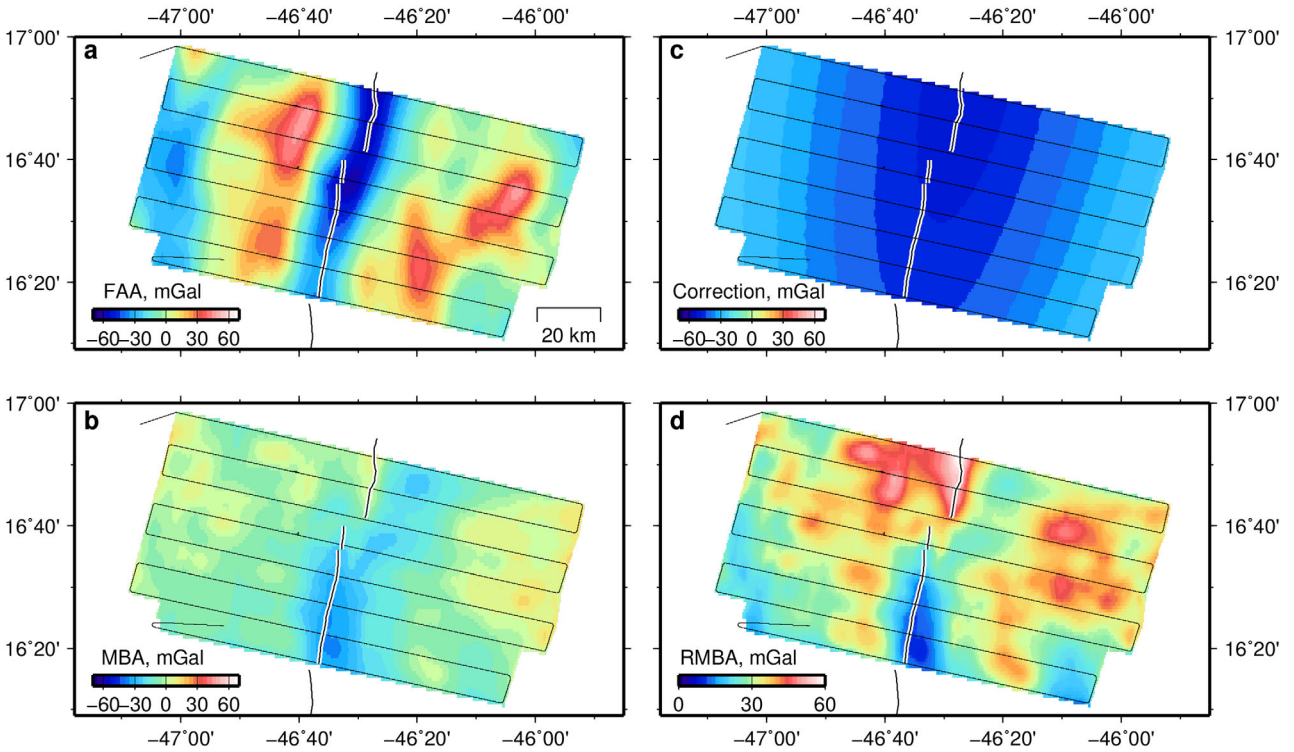

Figure 7. Gravity anomaly data reduction sequence, used to calculate residual crustal thickness (RCT; Figure 8). Thin black lines are shiptracks; black/white lines mark ridge axis. (a) Free-air anomaly (FAA) from KN210-05, gridded parallel to shiptrack to reduce artifacts. (b) Mantle Bouguer anomaly (MBA). (c) Gravitational contribution of passive mantle upwelling at ridge axis, calculated using three-dimensional model of *Phipps Morgan and Forsyth* [1988]. (d) Residual mantle Bouguer anomaly (RMBA), obtained from combining (b) and (c).

applied to wavelengths between 25 and 35 km. The signal was then downward continued to 8 km below sea level and the resulting map is shown in Figure 8a. Note that the 10 km trackline spacing of the survey means that features between tracklines are poorly constrained, therefore we restrict our interpretation accordingly.

5.2. RMBA and Relative Crustal Thickness

At the axis, the RMBA is higher in the north part of the study area than in the south where a large AVR has been constructed (Figure 7d). This axial low presumably reflects low density material concentrated locally beneath the ridge axis in the southern region. A distinct RMBA high is located at the northernmost part of the study area (Figure 7d), centered on the ridge axis and at least on line 2 appears to continue westward.

5.3. Crustal Structure

Crustal thickness is a useful first-order proxy for melt supply at the ridge axis [e.g., *McKenzie and Bickle*, 1988]. Thicker crust is expected at magmatic spreading centers, while thinner crust is expected in magma-starved regions such as inferred at segment ends [*Lin et al*., 1990; *Tucholke et al*., 1997]. Here we assume that variations in relative crustal thickness can be used to infer variations in melt supply (Figure 8a). Spreading-parallel profiles whose locations are marked in Figure 8a are plotted in Figures 8b and 8c. They show off-axis variations in relative crustal thickness. Along line 2 in the northern segment the spreading axis has a ~10 km wide relative crustal thickness low. This relative crustal thickness low is bounded on either side by regions of inferred thicker crust (Figure 8b). The +2 km relative crustal thickness located ~15 km east of the ridge axis along line 1 (marked A in Figure 8a) is the thickest part of a broader feature that extends over an area of ~25 km^2. This region appears to have the structural characteristics of typical, volcanic seafloor, with ~7 km thick crust, inward-facing normal fault scarps, and hummocky-looking seafloor topography. The relative crustal thickness anomaly on the conjugate side of the axis only reaches an amplitude of +1 km, although this anomaly has a similar areal extent to the crustal thickness high east of the axis (e.g., along line 2). The relative crustal thickness pattern in the southern area is markedly different (see along line 6, Figure 8c). Here the axis is characterized by a ~20 km-wide positive relative crustal

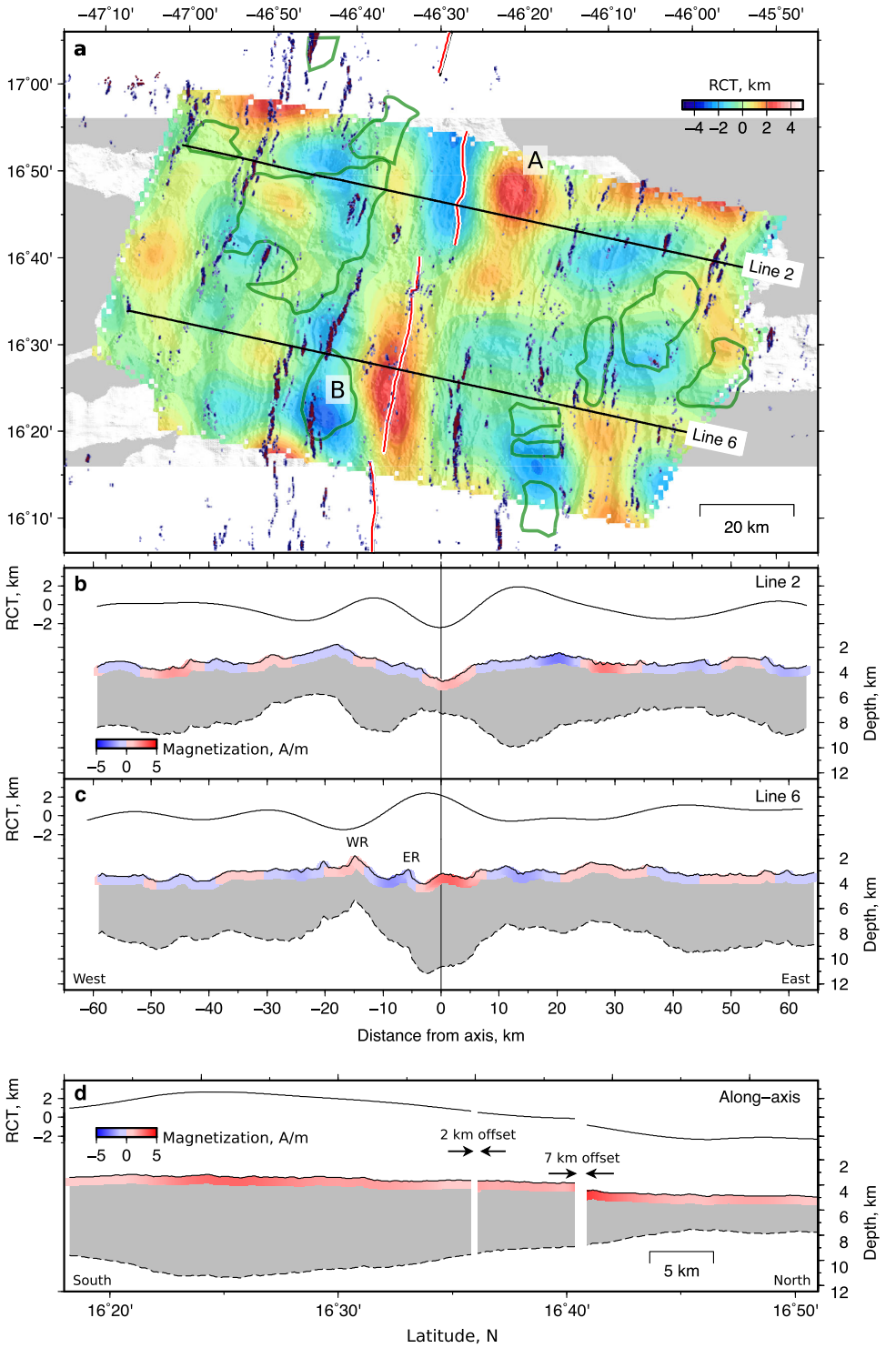

Figure 8. (a) Relative crustal thickness (RCT) with bathymetric shading. Red/white line marks ridge axis; green polygons are corrugated seafloor (following *Smith et al.* [2014]); colored dots mark outward-facing slopes with angle >20°. A and B show RCT anomalies discussed in text. (b and c) Profiles along line 2 and line 6, respectively. Upper solid line is RCT; lower solid line is bathymetry; dashed line/gray shading indicates depth to base of crust obtained from RCT grid assuming a reference crustal thickness of 5 km [*Escartin et al.*, 1999]. Blue/red strips show crustal magnetization profiles from Figure 4b; WR is West Ridge; ER is East Ridge. (d) Profile along ridge axis. Arrows indicate NTOs, offsets noted.

thickness anomaly, +2 km in amplitude. This positive anomaly is oriented subparallel to the ridge axis, approximately 10° from the present-day spreading trend. West of the axis is a pronounced relative crustal thickness low of −3 km along line 7 (marked B, Figure 8a), and coincides with the South Core Complex

detachment fault. This apparently thinned crust is present on both sides of the axis, although the anomaly is more pronounced to the west.

Along-axis variation in relative crustal thickness is shown in Figure 8d. The ridge axis in the southern area is dominated by a 30 km-long segment with relative crustal thickness of up to +3 km. Crust progressively thins along the axis north of 16°30′N, and defines an axis-parallel low that is bound on its southern edge by the NTO at 16°42′N. This relative crustal low has a minimum of −2 km. Hence we observe an apparent 5 km difference in axial crustal thickness from south to north across the area, over a distance of ∼55 km.

There appears to be a positive correspondence between the occurrence of exposed detachment fault scarps and relative crustal thickness (green polygons, Figure 8a). Areas of lowest relative crustal thickness coincide with exposed detachment surfaces, for example in the area marked B in Figure 8a, where the corrugated scarp of South Core Complex corresponds to a negative relative crustal thickness (−3 km). In contrast, no corrugated surfaces are associated with relative crustal thickness greater than approximately +1 km, suggesting that detachment faulting is not supported under these more magmatic conditions. This correlation supports the notion that detachment faulting is primarily an amagmatic process, during which preexisting lower crustal and upper mantle rocks are denuded to the seafloor [*John et al*., 2004; *Grimes et al*., 2008].

5.4. Tectonic Strain Estimates

We use observations of axis-facing slope angle to obtain quantitative estimates of tectonic strain, *T*, and thus indirectly of the proportion of plate separation accommodated by magmatic accretion, *M*, where $M = 1 - T$ [*Buck et al*., 2005; *Macleod et al*., 2009; *Mallows and Searle*, 2012]. Formation of detachment faults is most likely to occur when *M* is between 0.3 and 0.5 [*Tucholke et al*., 2008]. Tectonic strain can be estimated as the fraction of exposed fault scarp along profiles oriented parallel to the spreading direction. We calculate slopes angles along individual profiles extracted from the map in Figure 2b, sum the horizontal distances (apparent fault heaves) of inward facing slopes $>10^{\circ}$ and normalize by profile length [*Escartin et al*., 1999; *Paulatto et al*., 2015]. We acknowledge that the choice of slopes $>10^{\circ}$ will include some volcanic slopes, however additional data (e.g., near-bottom sidescan sonar images) to resolve this issue are not available. Profiles are restricted to crust <1.5 Ma in age (∼16 km either side of the spreading axis), in order to minimize the effects of sedimentation. In addition, we ignore the effects of mass-wasting and assume that fault slip is parallel to the spreading direction. We analyzed 150 profiles spaced 200 m apart in the ridge-parallel direction, eight of which coincide with ship tracks of Cruise KN210-05; these eight profiles are shown in Figure 9a. The resulting time-averaged estimates of *T* and *M* in Figure 9b do not represent the actual tectonic strain at any one time, which may have changed substantially during the 1.5 Ma period in question. Furthermore, our estimates of *M* carry considerable uncertainty as there may be fault scarps with slope $<10^{\circ}$ which are incorrectly categorized as magmatic seafloor in our analysis, or conversely there may be magmatic terrain with slope $>10^{\circ}$ assumed to be fault scarps.

Values of *M* vary between 0.1 and 0.65 across the study area. We find that the majority of the study area has *M* between 0.3 and 0.5, consistent with the formation and maintenance of oceanic core complexes [*Tucholke et al*., 2008]. Values of *M* to the north of the NTO at 16°42′N are typically lower (<0.4) than those in the south, indicating that the majority of the seafloor is being formed by faulting there although we have not identified an active core complex north of the NTO [*Smith et al*., 2014]. In the south, *M* is typically higher, with two ridge sections centered at 16°20′N and 16°30′ N showing local highs of >0.5. Hence we infer increased magmatism in the south of the study area even though this region has active detachment faulting along most of the western boundary fault. Note that south of the Southern core complex, near 16°10′N, *M* is < 0.4.

We use our estimates of relative crustal thickness as a second method to independently assess variations in *M* and *T*. The inferred percentage of magmatic accretion at any point, *M*, can be written as

$$M = \frac{(tc_r + tc_{ref})M_{mag}}{tc_{mag}} \quad (1)$$

where tc_r is relative crustal thickness, $tc_{ref} = 5$ km is the reference crustal thickness used in downward continuation of RMBA, $M_{mag} = 0.80$ is the assumed proportion of spreading accommodated by magmatism at a magma-rich slow-spreading center [*Escartin et al*., 1999] and $tc_{mag} = 7.1$ km is the typical crustal thickness

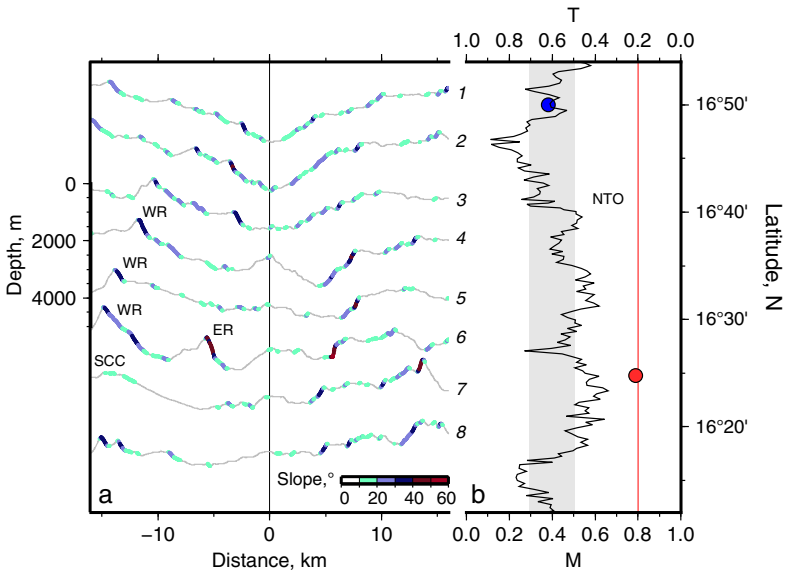

Figure 9. Bathymetric slope and tectonic strain estimates. (a) Bathymetric profiles 1–8, shaded where slope >10°, locations shown in Figure 1. WR, ER, and SCC indicate locations of West Ridge, East Ridge and South Core Complex, respectively. (b) Solid black line is variation in tectonic strain, T (or $M = 1 - T$), from 150 bathymetric profiles as a function of latitude. Gray band shows range of M values associated with detachment faulting [*Tucholke et al.*, 2008]; red line indicates typical M value for magmatic spreading [*Escartin et al.*, 1999]; red and blue dots are values of M from relative crustal thickness estimates, NTO shows latitude of nontransform offset.

at a magma-rich slow-spreading center. Using equation (1), the relative crustal thickness of +2 km observed at the ridge axis in the south of the study area near 16°25′N corresponds to M of 0.78. For comparison, *Mallows and Searle* [2012] used a similar approach in the area of detachment faulting near 13°N at the MAR and obtained a minimum estimate of M of 0.56. This contrasts with the area to the north at 16°50′N, where relative crustal thickness of −2 km corresponds to M of 0.38.

Our two independent estimates of M are in broad agreement in that they show a trend of increasing magmatism from north to south. M obtained from the relative crustal estimate in the north at 16°50′N matches well with that obtained from bathymetric slopes. To the south, M estimated from relative crustal thickness near 16°25′N is much higher than that from bathymetric slope profiles (Figure 9b), reflecting the degree of uncertainty in each method. Moreover, since active detachment faulting has been identified in the southern region, we would assume that M would not be >0.5 in this area, therefore our approach may reflect an overestimate. Despite these uncertainties, our observations show that faulting is important throughout this area, in particular in the northern segment where magmatic processes accommodate relatively less strain associated with plate spreading.

6. Discussion

6.1. Axial Tectonic Structure

The bathymetric, magnetic and gravity data in the 16°30′N region presented here reveal a systematic pattern along the ridge axis. In the southern part of the study area the ridge axis is shallow (∼3400 m adjacent to SCC) and characterized by a robust AVR. The ridge axis deepens toward the north and water depths average ∼4500 m north of the NTO near 16°42′N. Volcanic activity is sparse and an AVR is absent in the northern segment [*Smith et al.*, 2014]. This first-order variation in axial depth and morphology is accompanied by changes in the magnetic and gravity signals. In the south, between 16°30′N and 16°40′N, the ridge axis is characterized by a high central anomaly magnetization intensity (Figure 4). North of the NTO at 16°42′N, the central anomaly magnetization is reduced in amplitude. RMBA and relative crustal thickness estimates show similar along-axis variability. Low RMBA and high relative crustal thickness (+3 km) are observed in the south. In the deeper, northern area, RMBA is higher and relative crustal thickness is −2 km.

Together, these observations suggest two distinct modes of spreading at the present day. In the south, volcanism and magma supply are sufficient enough to produce an AVR, and generate crust which is

comparable to the global, seismically determined average of 7.1 ± 0.8 km [*White et al*., 1992]. A typical, magmatically controlled magnetic source layer would explain the strong positive central anomaly with amplitude >200 nT. In the north, volcanism and magma supply are probably weaker [*Smith et al*., 2014]. Here no AVR has formed and the crust is estimated to be 3–5 km thick. The associated magnetic layer is estimated to be thin, and results in reduced central magnetic anomaly amplitude.

Thickened crust located 15 km east of the ridge axis in the north (A, Figure 8a) is in sharp contrast to the thin crust apparently being accreted at the axis today. This change in crustal thickness takes place over only ~15 km, and is ~4 km in magnitude (Figure 8b). The short wavelength of this feature suggests a considerable change in magma supply over a short time period, probably only ~1.5–2.0 million years. Therefore the magmatically anemic spreading center at the north of the study area may be a recent feature, prior to which magmatic accretion played a more important role.

6.2. Tectonic Reorganization

Misalignment between modern-day volcanic spreading center and magnetic anomalies indicates tectonic reorganization of the axis within the past 780 ka. The present axis trends ~005° and has a right-lateral NTO of ~7 km. In contrast, the Brunhes-Matuyama boundary (780 ka) and older magnetic anomalies trend ~010° and show no evidence of an offset (Figure 4b). Bathymetric lineations, including fault scarps, on the eastern flank are also oriented parallel to the magnetic anomaly trends. These features also show no evidence of a past offset of the axis. These observations suggest that prior to ~780 ka, the spreading axis was continuous and unbroken without offset, trending ~010°. A reorganization of the axis is likely to have taken place between ~780 ka and today, which created the relatively young NTO at 16°42′N. This reorganization may have taken the form of variable asymmetric spreading, subtle ridge jumps or rift propagation. Since the reorganization took place after 780 ka, there are no magnetic reversal markers to provide a record of its history.

6.3. Central Anomaly Magnetization

The positive magnetization, associated with the central Bruhnes anomaly, has an asymmetrical distribution relative to the axis. This positive signal is consistently located 2–4 km to the east of the volcanic axis axis (Figures 4 and 5). Furthermore, the mean width of the central magnetic anomaly is 10.0 km, ~40% narrower than the 16.4 km width that would typically be expected at an average spreading rate of 21.2 km Ma^{-1}. The width of the central anomaly also shows variation between profiles, ranging from 8 km on line 7 up to 12 km on line 5. This 3–6 km length scale in variability is similar to that observed south of the Fifteen-Twenty Fracture Zone [*Fujiwara et al*., 2003; *Mallows and Searle*, 2012]. This scale of heterogeneity may reflect lithological heterogeneity between peridotite and gabbro intrusions, altered by varying degrees of serpentinization [*Blackman et al*., 2002; *Karson et al*., 2006; *Dick et al*., 2008; *Mallows and Searle*, 2012].

The across-axis asymmetry in the central Bruhnes anomaly could be explained by two mechanisms. First, a recent westward shift in the locus of magmatic accretion could cause the magmatic axis to become misaligned with the magnetization signature of slightly older crust in the northern segment. This process is consistent with the location of the NTO at 16°42′N, which appears to be associated with a change in the degree of magnetization asymmetry along line 3. Second, variations in magnetization associated with lithological boundaries could give rise to an asymmetric central anomaly (Figure 10). Asymmetric accretion mode, with magmatic spreading to the east and detachment-mode spreading to the west, is likely to play an important role in this area. This spreading mode may cause highly magnetized basalt crust spread to the east and weakly magnetized rift-valley infill to the west (Figure 10). This rift-valley to the west is the hanging wall of the detachment fault, and has not been spread away since the fault developed, leaving a crustal sliver behind [*Allerton et al*., 2000]. This sliver is likely to be composed of basalt flows piled on top of each other (perhaps with alternating magnetization directions resulting in a weak net magnetization) as well as mass-wasted material supplied from off-axis slopes. Since hydrothermal systems are commonly associated with detachments the hanging wall is probably highly altered by hydrothermal circulation [*McCaig et al*., 2007]. U-Pb zircon ages from Atlantis Massif suggest that the crust itself may comprise a series of small-scale sills which intrude into one another over length scales of ~1.4 km, which would result in an irregular magnetic anomaly pattern [*Grimes et al*., 2008]. Hence the magnetization of the hanging wall adjacent to a detachment fault may be considerably reduced. In addition to this poorly magnetized material, the rotation associated with detachment slip may further distort the magnetic signal.

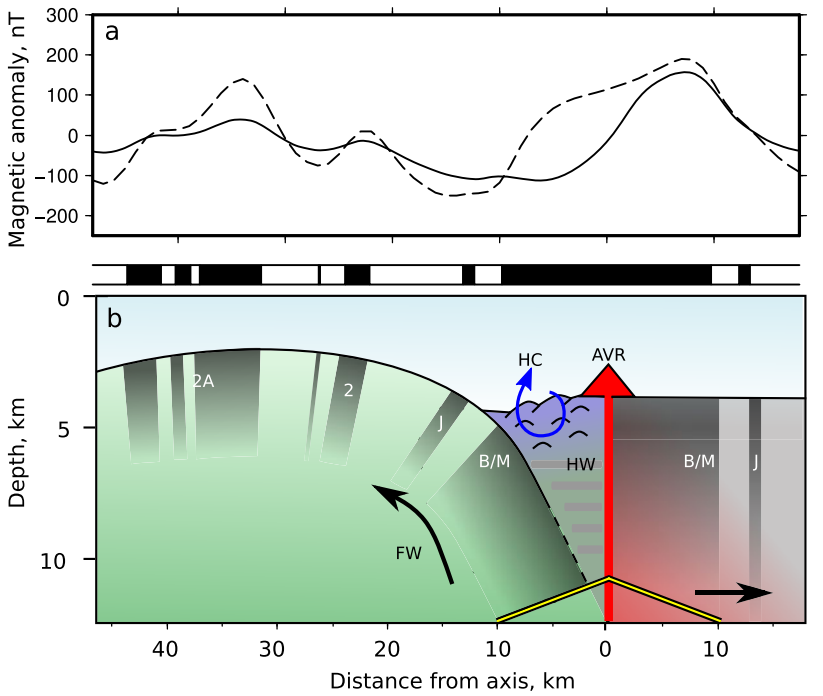

Figure 10. Cartoon illustrating asymmetric shape of central magnetic anomaly. (a) Sketch of observed magnetic anomaly profile over spreading axis in study area. Dashed line shows typically observed magnetic anomaly; solid line shows observed anomaly with reduced signal of the Bruhnes-Matuyama reversal and off-axis. (b) Simplified crustal structure, black arrows show spreading direction. Red line/triangle is axis/axial volcanic ridge (AVR); gray/red shaded block shows magmatic upper crust; labeled vertical/rotated gray blocks are magnetized bodies (B/M is Bruhnes-Matuyama; J is Jaramillo); yellow line is Curie isotherm; green shaded block shows upper/lower crust of detachment fault footwall (FW); blue arrow is hydrothermal circulation (HC); horizontal gray/blue shading with black hummocks represents rift valley infill within hanging wall (HW).

The consistent clockwise phase shift between observed and calculated magnetic anomalies east of the axis implies suggests the rotation of magnetized bodies. This finding is in agreement with *Mallows and Searle* [2012], who found that the observed axial magnetization at 13°N can be explained by a 45° westward rotation of the magnetization vector. The weakly magnetized upper and lower crustal gabbros are also likely to be rotated as slip on a detachment continues, further distorting magnetic anomalies over low-angle detachments.

6.4. Detachment Fault Activity

Regional and high-resolution bathymetric and sidescan sonar data demonstrate that detachment faulting plays a major role in crustal accretion in the 16°30′N area [*Smith et al.*, 2014]. Large portions of the seafloor on both sides of the spreading axis show a terrain typical of detachment faulting (Figure 2d). The tapered distribution of sediment on footwall outcrops also suggests that these faults are active today [*Parnell-Turner et al.*, 2014]. These detachments represent rotated footwalls of low-angle faults, which probably began as normal faults. On the western side of the axis, *Smith et al.* [2014] identified ~10 km long lineations oriented parallel to the spreading direction. They interpreted these lineations as large-scale corrugations, formed during slip along long-lived detachment faults. The widespread nature of these lineations led *Smith et al.* [2014] to conclude that detachment faulting has dominated the west flank of the axis for the past 5 Ma. Detachment faulting is also indicated by lineations on crust >2 Ma on the eastern flank [*Smith et al.*, 2014].

The common occurrence of detachments is consistent with our observation of lower than expected magnetization to the west of the axis (Figures 8 and 10). The ubiquitous presence of detachment faults both along axis and over the past 5 Ma can also explain the difference in magnetization on either side of the ridge axis we have documented here. Regions of corrugated seafloor appear to mostly coincide with areas of negative relative crustal thicknesses (e.g., region marked B, Figure 8a). Areas with relative crustal thickness >1 km do not show evidence for corrugations, and also tend to have fewer outward-facing fault scarps (e.g., region marked A, Figure 8a). Areas of corrugated seafloor and low relative crustal thickness identified here are in

good agreement with the lithology of rock samples dredged near the ridge axis (<20 km), where gabbro and peridotite samples were documented by *Smith et al*. [2014]. The presence of these lithologies at the seafloor is indicative of slip on detachment faults bringing lower crustal and mantle rocks to the surface. The identification of near-axis detachment faults confirmed by geological sampling adds confidence to our interpretation that features further off-axis (>20 km), where we do not have dredge samples, are also detachment-fault related.

7. Conclusions

Earthquake seismicity, bathymetry, gravity, magnetic and dredging surveys show that the 16°30′N area of the MAR is an area of active detachment faulting. Total spreading rate is 21.2 km Ma^{-1}, slower than that previously reported near the Fifteen-Twenty Fracture Zone, although supported by our magnetic models and regional magnetic profiles. Crustal magnetization is generally lower in amplitude west of the axis, and the central anomaly is 40% narrower than expected with no anomaly present west of the volcanic axis. The central anomaly appears to be typically developed to the east of the volcanic axis on all profiles. The shape of the central anomaly may be explained by a low-magnetized hanging wall adjacent to active detachment faults. Lithological variations caused by detachment faulting may lead to highly magnetized young basalts east of the axis to be juxtaposed with the weakly magnetized old lava flows and products of mass-wasting that fill the axial valley to the west. Finally, older basalt flows subjected to increased hydrothermal circulation may cause a subdued magnetic anomaly. This combination of rotation, lithological juxtaposition and hydrothermal alteration can explain the asymmetrical central magnetization pattern observed here. Misalignment between modern-day volcanic spreading center and off-axis magnetic anomalies and bathymetry indicate a tectonic reorganization of the axis within the past 780 ka. This reorganization may have taken the form of variable asymmetric spreading or ridge jumps or rift propagation but since it happened after 780 ka there are no magnetic reversal markers to trace its history.

Gravity data indicate relatively thick crust in the south, thinning to the north. This is reflected by a change in axial morphology. In the south segment the median valley floor is ~10 km wide, a large AVR has been constructed, and water depths average ~3500 m In the northern segment, the valley floor is narrow (~3–4 km wide), a prominent AVR has not developed, indicating anemic volcanism, and water depths average ~4500 m. Off-axis changes in calculated relative crustal thickness suggest a rapid (1–2 Ma) transition from normal thickness magmatic crust to very thin crust at the current ridge axis in the north segment. We have observed short length scale variations in magnetization, crustal architecture and bathymetry in this region. These spatially short wavelength patterns indicate that the processes controlling crustal accretion in these settings act over short timescales (1–2 Ma).

Acknowledgments

Bathymetric, gravity and magnetic data are available online at http://www.rvdata.us/catalog/KN210-05. This work was supported by the National Science Foundation grant number OCE-1155650. We are grateful to the captain, crew and science party of R/V *Knorr* for their professionalism and hard work during Cruise KN210-05. We thank D. Blackman, J. Escartin, M. Ligi, C. Palmiotto, M. Tivey and B. Tucholke for their helpful comments. Figures prepared using the Generic Mapping Tools [*Wessel and Smith*, 1998]. We are grateful for the comments from T. Fujiwara and an anonymous reviewer which improved this paper.

References

Allerton, S., J. Escartin, and R. C. Searle (2000) Extremely asymmetric magmatic accretion of oceanic crust at the ends of slow-spreading ridge segments, *Geology*, *28*, 179–182.

Baines, A. G., M. J. Cheadle, B. E. John, and J. J. Schwartz (2008) The rate of oceanic detachment faulting at Atlantis Bank, SW Indian Ridge, *Earth Planet. Sci. Lett.*, *273*, 105–114.

Blackman, D. K., et al. (2002), Geology of the Atlantis Massif (Mid-Atlantic Ridge, 30°N): Implications for the evolution of an ultramafic oceanic core complex, *Mar. Geophys. Res.*, *23*, 443–469.

Buck, W. R. (1988), Flexural rotation of normal faults, *Tectonics*, *7*, 959–973.

Buck, W. R., L. L. Lavier, and A. N. B. Poliakov (2005), Modes of faulting at mid-ocean ridges, *Nature*, *434*, 719–723.

Cande, S. C., and Kent, D. V. (1995), Revised calibration of the geomagnetic polarity timescale for the Late Cretaceous and Cenozoic, *J. Geophys. Res.*, *100*, 6093–6095.

Cann, J. R., D. K. Blackman, D. K. Smith, E. McAllister, B. Janssen, S. Mello, E. Avgerinos, A. R. Pascoe, and J. Escartin (1997), Corrugated slip surfaces formed at North Atlantic ridge-transform intersections, *Nature*, *385*, 329–332.

Cannat, M., et al. (1995), Thin crust, ultramafic exposures, and rugged faulting patterns at the Mid-Atlantic Ridge (22°–24°N), *Geology*, *23*, 49–52.

Cannat, M., D. Sauter, V. Mendel, E. Ruellan, K. Okino, J. Escartin, V. Combier, M. Baala, and M. Balaa (2006), Modes of seafloor generation at a melt-poor ultraslow-spreading ridge, *Geology*, *34*, 605–608.

Caress, D. W., and D. L. Chayes (1996), Improved processing of hydrosweep DS multibeam data on the R/V Maurice Ewing. *Mar. Geophys. Res.*, *18*, 631–650.

DeMets, C., R. G. Gordon, D. F. Argus, and S. Stein (1990), Current plate motions, *Geophys. J. Int.*, *101*, 425–478.

DeMets, C., R. G. Gordon, and D. F. Argus (2010), Geologically current plate motions, *Geophys. J. Int.*, *181*, 1–80.

Dick, H. J. B., M. A. Tivey, and B. E. Tucholke (2008), Plutonic foundation of a slow-spreading ridge segment: Oceanic core complex at Kane Megamullion, 23°30′N, 45°20′W, *Geochem. Geophys. Geosyst.*, *9*, Q05014, doi:10.1029/2007GC001645.

Escartin, J., P. A. Cowie, R. C. Searle, S. Allerton, N. C. Mitchell, C. J. Macleod, and P. A. Slootweg (1999), Quantifying tectonic strain and magmatic accretion at a slow spreading ridge segment, Mid-Atlantic Ridge, 29°N, *J. Geophys. Res.*, *104*, 10,421–10,437.

Escartin, J., D. K. Smith, J. R. Cann, H. Schouten, C. H. Langmuir, and S. Escrig (2008), Central role of detachment faults in accretion of slow-spreading oceanic lithosphere, *Nature*, *455*, 790–794.

Finlay, C. C., et al. (2010) International Geomagnetic Reference Field: The eleventh generation. *Geophys. J. Int.*, *183*, 1216–1230.

Fujiwara, T., J. Lin, T. Matsumoto, P. B. Kelemen, B. E. Tucholke, and J. F. Casey (2003), Crustal evolution of the Mid-Atlantic Ridge near the fifteen-twenty fracture zone in the last 5 Ma, *Geochem. Geophys. Geosyst.*, *4(5)*, 1024, doi:10.1029/2002GC000364.

Grimes, C. B., B. E. John, M. J. Cheadle, and J. L. Wooden (2008), Protracted construction of gabbroic crust at a slow spreading ridge: Constraints from 206Pb/238U zircon ages from Atlantis Massif and IODP Hole U1309D (30°N, MAR), *Geochem. Geophys. Geosyst.*, *9*, Q08012, doi:10.1029/2008GC002063.

John, B. E., D. A. Foster, J. M. Murphy, M. J. Cheadle, A. G. Baines, C. M. Fanning, and P. Copeland P. (2004), Determining the cooling history of in situ lower oceanic crust-Atlantis Bank, SW Indian Ridge, *Earth Planet. Sci. Lett.*, *222*, 145–160.

Karson, J. A. (1999), Geological investigation of a lineated massif at the Kane Transform Fault: Implications for oceanic core complexes, *Philos. Trans. R. Soc. London A*, *357*, 713–736.

Karson, J. A., Fruh-G. L. Green, D. S. Kelley, E. A. Williams, D. R. Yoerger, and M. Jakuba (2006), Detachment shear zone of the Atlantis Massif core complex, Mid-Atlantic Ridge, 30°N, *Geochem. Geophys. Geosyst.*, *7*, Q06016, doi:10.1029/2005GC001109.

Kuo, B.-Y., and D. W. Forsyth (1988), Gravity anomalies of the ridge-transform system in the South Atlantic between 31 and 34.5 S: Upwelling centers and variations in crustal thickness, *Mar. Geophys. Res.*, *10*, 205–232.

Lagabrielle, Y., D. Bideau, M. Cannat, J. A. Karson, and C. Mevel (1998), Ultramafic-mafic plutonic rock suites exposed along the Mid-Atlantic Ridge (10°N–30°N): Symmetrical-asymmetrical distribution and implications for seafloor spreading processes, in *Faulting and Magmatism at Mid-Ocean Ridges*, edited by W. R. Buck, pp. 153–176, AGU, Washington, D. C.

Lin, J., G. M. Purdy, H. Schouten, J.-C. Sempere, and C. Zervas (1990) Evidence from gravity data for focused magmatic accretion along the Mid-Atlantic Ridge, *Nature*, *344*, 627–632.

Macleod, C. J., et al. (2002), Direct geological evidence for oceanic detachment faulting: The Mid-Atlantic Ridge, 15 45′ N, *Geology*, *30*, 879–882.

Macleod, C. J., R. C. Searle, B. J. Murton, J. F. Casey, C. Mallows, S. C. Unsworth, K. L. Achenbach, and M. Harris (2009) Life cycle of oceanic core complexes, *Earth Planet. Sci. Lett.*, *287*, 333–344.

Mallows, C., and R. C. Searle (2012), A geophysical study of oceanic core complexes and surrounding terrain, Mid-Atlantic Ridge 13°N-14°N, *Geochem. Geophys. Geosyst.*, *13*, doi:10.1029/2012GC004075.

McCaig, A. M., R. Cliff, J. Escartin, A. Fallick, and C. J. Macleod (2007), Oceanic detachment faults focus very large volumes of black smoker fluids, *Geology*, *35*, 935.

McKenzie, D. P., and M. J. Bickle (1988), The volume and composition of melt generated by extension of the lithosphere, *J. Petrol.*, *29*, 625–679.

Mendel, V., M. Munschy, and D. Sauter (2005), MODMAG, a MATLAB program to model marine magnetic anomalies, *Comput. Geosci.*, *31*, 589–597.

Micallef, A., C. Berndt, D. G. Masson, and D. A. V. Stow (2007), A technique for the morphological characterization of submarine landscapes as exemplified by debris flows of the Storegga Slide, *J. Geophys. Res.*, *112*, F02001, doi:10.1029/2006JF000505.

Nabighian, M. N. (1972), The analytic signal of two-dimensional magnetic bodies with polygonal cross-section: Its properties and use for automated anomaly interpretation, *Geophysics*, *37*, 507–517.

Okino, K., K. Matsuda, D. M. Christie, Y. Nogi, and K. Koizumi (2004), Development of oceanic detachment and asymmetric spreading at the Australian-Antarctic Discordance, *Geochem. Geophys. Geosyst.*, *5*, Q12012, doi:10.1029/2004GC000793.

Parker, R. (1973), The rapid calculation of potential anomalies, *Geophys. J. Int.*, *31*, 447–455.

Parker, R. L., and S. Huestis (1974) The inversion of magnetic anomalies in the presence of topography, *J. Geophys. Res.*, *79*, 1587–1593.

Parnell-Turner, R., J. R. Cann, D. K. Smith, H. Schouten, D. Yoerger, C. Palmiotto, A. Zheleznov, and H. Bai (2014), Sedimentation rates test models of oceanic detachment faulting, *Geophys. Res. Lett.*, *41*, 7080–7088, doi:10.1002/2014GL061555.

Paulatto, M., J. P. Canales, R. A. Dunn, and R. A. Sohn (2015), Heterogeneous and asymmetric crustal accretion: New constraints from multibeam bathymetry and potential field data from the Rainbow area of the Mid-Atlantic Ridge (36°15′N), *Geochem. Geophys. Geosyst.*, *16*, 2994–3014, doi:10.1002/2015GC005743.

Peter, G., O. E. Dewald, and B. G. Bassinger (1973), Caribbean Atlantic Geotraverse, NOAA-IDOE 1971, Report No. 2, Magnetic Data, *NOAA Tech. Rep. ERL 288-AOML 12*, pp. 1–7, Environmental Research Laboratories, Boulder, Colo.

Phipps Morgan, J., and D. W. Forsyth (1988), Three-dimensional flow and temperature perturbations effects on oceanic crustal and upper mantle structure, *J. Geophys. Res.*, *93*, 2955–2966.

Prince, R. A., and D. W. Forsyth (1988), Horizontal extent of anomalously thin crust near the Vema Fracture Zone from the three-dimensional analysis of gravity anomalies, *J. Geophys. Res.*, *93*, 8051–8063.

Roest, W. R., and B. J. Collette (1986), The fifteen twenty fracture zone and the North American-South American plate boundary, *J. Geol. Soc.*, *143*, 833–843.

Schroeder, T., and M. Cheadle (2007) Nonvolcanic seafloor spreading and corner-flow rotation accommodated by extensional faulting at 15 N on the Mid-Atlantic Ridge: A structural synthesis of ODP Leg 209, *Geochem. Geophys. Geosyst.*, *8*, Q06015, doi:10.1029/2006GC001567.

Searle, R. C., M. Cannat, K. Fujioka, C. Mevel, H. Fujimoto, A. Bralee, and L. Parson (2003), FUJI Dome: A large detachment fault near 64°E on the very slow-spreading southwest Indian Ridge, *Geochem. Geophys. Geosyst.*, *4*(8), 9105, doi:10.1029/2003GC000519.

Smith, D. K., J. Escartin, M. Cannat, M. Tolstoy, C. G. Fox, D. R. Bohnenstiehl, and S. Bazin (2003) Spatial and temporal distribution of seismicity along the northern Mid-Atlantic Ridge (15°–35°N), *J. Geophys. Res.*, *108*(B3), 2167, doi:10.1029/2002JB001964.

Smith, D. K., J. R. Cann, and J. Escartin (2006), Widespread active detachment faulting and core complex formation near 13°N on the Mid-Atlantic, *Nature*, *442*, 440–443.

Smith, D. K., J. Escartin, H. Schouten, and J. R. Cann (2008), Fault rotation and core complex formation: Significant processes in seafloor formation at slow-spreading mid-ocean ridges (Mid-Atlantic Ridge, 13°–15°N), *Geochem. Geophys. Geosyst.*, *9*, Q03003, doi:10.1029/2007GC001699.

Smith, D. K., et al. (2014), Development and evolution of detachment faulting along 50 km of the Mid-Atlantic Ridge near 16.5°N, *Geochem. Geophys. Geosyst.*, *15*, 4692–4711, doi:10.1002/2014GC005563.

Tisseau, J., and P. Patriat (1981), Identification des anomalies magnétiques sur les dorsales à faible taux d'expansion: Méthode des taux fictifs, *Earth Planet. Sci. Lett.*, *52*, 381–396.

Tucholke, B. E., and J. Lin (1994), A geological model for the structure of ridge segments in slow spreading ocean crust, *J. Geophys. Res.*, *99*, 11,937–11,958.

Tucholke, B. E., J. Lin, M. C. Kleinrock, A. Tivey, B. Reed, and G. E. Jaroslow (1997), Segmentation and crustal structure of the western Mid-Atlantic Ridge flank, 25°25′ - 27°10′ N and 0-29 m.y, *J. Geophys. Res.*, *102*, 10,203–10,223.

Tucholke, B. E., J. Lin, and M. C. C. Kleinrock (1998), Megamullions and mullion structure defining oceanic metamorphic core complexes on the Mid-Atlantic Ridge, *J. Geophys. Res.*, *103*, 9857–9866.

Tucholke, B. E., M. Behn, W. R. Buck, and J. Lin (2008), Role of melt supply in oceanic detachment faulting and formation of megamullions, *Geology*, *36*, 455.

Wessel, P., and W. H. F. Smith (1998), New, improved version of generic mapping tools released, *Eos Trans. AGU*, *79*, 579.

White, R. S., D. P. McKenzie, and R. K. O'Nions (1992) Oceanic crustal thickness from seismic measurements and rare earth element inversions, *J. Geophys. Res.*, *97*, 19,683–19,715.